ACS OMEGA

Open Access

http://pubs.acs.org/journal/acsodf

Article

Foam Generation Through a Single Pore with Rectangular Cross-Section: Hysteretic Behavior and Geometric Limitation of the Volume Fraction of Bubbles

Mattéo Clerget,* Alexandra Klimenko, Maurice Bourrel, François Lequeux, and Pascal Panizza

Cite This: *ACS Omega* 2024, 9, 8320−8332

Read Online

ACCESS | Metrics & More | Article Recommendations

ABSTRACT: We study foam production and destabilization through a flow-focusing geometry, namely a single pore of rectangular cross-section, by coinjecting gas and liquid at constant pressure, P_g, and constant flow rate, Q_w. We observe that bubble production results from a Rayleigh-Plateau destabilization of the internal gas thread that occurs at the pore neck when its width becomes comparable to the height of the rectangular-section channel. Using a simple model and numerical approach, we (i) predict the shape of the gas jet and its stability range as a function of flow parameters and device geometry, which we successfully compare with our experimental results, and (ii) demonstrate the existence of a critical local pressure drop at the pore neck that determines whether or not a stable gas flow can form. We thus show that bubble foam generation exhibits hysteretic behavior due to hydrodynamic feedback and demonstrate that there is a maximum bubble volume fraction that the generated foam cannot exceed, the value of which is fixed by the geometry. Our results suggest that the foam collapse observed in porous media when the fractional gas flow becomes too large may result from hydrodynamic feedback inhibiting foam generation and not necessarily from coalescence between bubbles, as is usually claimed.

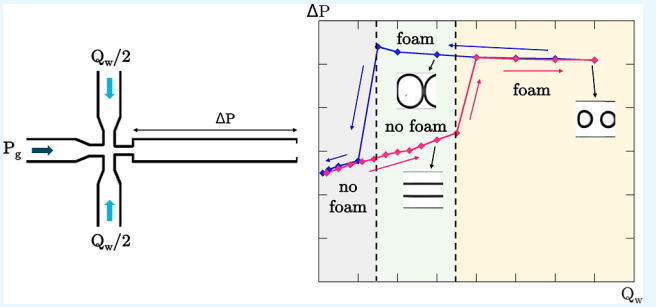

1. INTRODUCTION

Foam injection in porous media is a process that is used in many applications such as EOR (enhanced oil recovery), soils remediation or CO_2 sequestration, to name a few of them.[1,2] An effective EOR strategy consists of injecting aqueous foams, based on CO_2 or other gases, into oil reservoirs.[3,4] This approach has several advantages over conventional injection methods using either gas or surfactant solutions. The foam reduces the mobility of the injection fluids by increasing its viscosity and reducing the relative permeability[3,5,6] which makes possible to limit the effects of viscous fingerings within the porous matrix and therefore to increase the recovery efficiency. Furthermore, the presence of bubbles contained in the foam blocks certain passages in the porous medium,[7] thus locally increases the hydrodynamic pressure in the neighboring pores, for a given injection flow rate, and therefore displaces oil droplets initially trapped in these pores. In both cases -sequestration or recovery-, this effect considerably increases the number of preferential paths explored in the porous matrix by the injected gas,[8] thus significantly improving the sweeping efficiency and potentially the fraction of oil recovered or gas trapped, i.e., stored. Although this injection strategy is very promising in terms of results, its use, however, remains relatively limited because its implementation requires control of both the in situ generation and stability of a foam at reservoir conditions. While the rules to obtain a stable and viscous foam are well-known in bulk,[9] these issues still remain very elusive in a porous medium.[10]

First of all, in contrast to bulk foams for which gravity drainage and gas diffusion are the main destruction processes, coalescence becomes the predominant destruction factor for foams in porous media. Furthermore, the steady state texture of the foam results from a subtle population balance between destruction and flow-induced creation processes.[5,6,11] As a consequence, the rheology of foam in porous media totally differs from that determined in bulk experiments, with usually much larger viscosities because of the confinement of the foam bubbles.[12] When coinjecting gas and liquid in a porous medium with respective flow rates, Q_g and Q_w, two macroscopic regimes are observed depending on the gas fractional flow, $f_g = \frac{Q_g}{Q_g + Q_w}$.[5] Below $f_g \leq f_g^*$, in the so-called low quality foam regime, the effective viscosity of the foam, which exhibits a strongly shear

Received: November 14, 2023
Revised: January 6, 2024
Accepted: January 24, 2024
Published: February 7, 2024

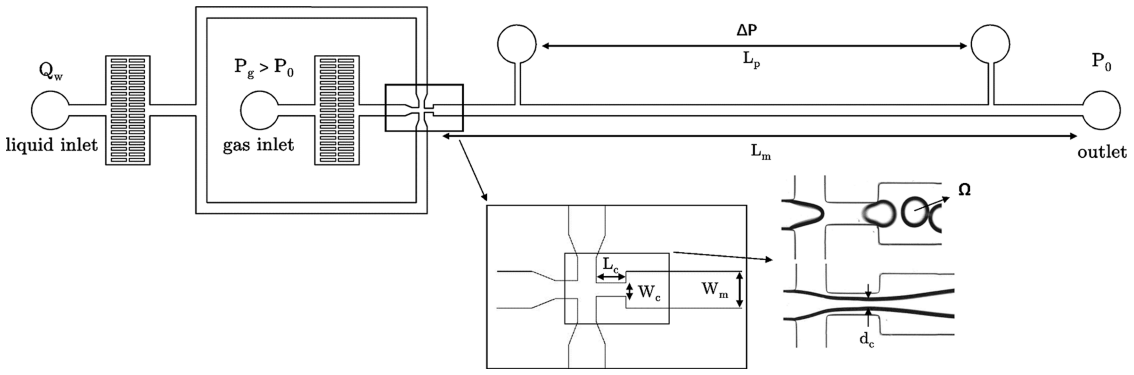

Figure 1. Schematic top view of the microfluidic device used to study the generation of foam and definition of its geometric parameters. Inset: Details of the FFG. The width of W_m of the main channel is always 400 μm, whereas L_p = 1.7 cm and L_m = 2.35 cm. The length of the constriction is L_c = 600 μm, and its width W_c is either 100, 200, or 250 μm. The height of the channels is 76 μm. Inset: Images of the flow in the jet and in the bubble regime.

thinning behavior, scales with the capillary number $C_a = \frac{\eta_w V}{\gamma}$ (η_w, γ, and V being respectively the liquid viscosity, the gas/liquid surface tension, and the mean gas velocity), as C_a^{-n} with n a value that is in the $[0.75-1]$ range, and it is a monotonic increasing function of f_g.[13,14] At f_g^*, the effective viscosity drops sharply because of the sudden formation of continuous pathways along which the gas preferentially flows. This collapse of the foam is usually attributed to coalescence events because as the foam becomes drier, the capillary pressure that increases may exceed a limiting capillary pressure[15] beyond which coalescence events occur. This limiting capillary pressure varies with surfactant formulation, gas velocity, and permeability of the medium. However, these variations are still not fully understood. As the formation of low quality foams, witnessed for $f_g \geq f_g^*$, is very detrimental for industrial applications, a key issue is therefore to rationalize this phenomenon. Such a task is in fact necessary to screen the formulation of the surfactant solutions that are to be coinjected[10,16−18] and thus looking for increasing f_g^* while optimizing foam viscosity.

To answer this question, we study foam generation and destabilization through a single microfluidic pore by coinjecting gas and liquid at constant pressure, P_g, and constant flow rate, Q_w, respectively. Taking advantage of our transparent 2D setup, fabricated using standard poly dimethylsiloxane soft lithography methods,[19] we can image the structure of the two phase flow in situ and then relate it to its effective viscosity. Such a methodology has proved particularly suitable for studying the flow of confined foams at the scale either of a single bubble or of an assembly of bubbles. At the bubble scale, it allows one to directly observe the dynamic of gas snap-off[20] or bubble−bubble pinch-off[21] mechanisms. At the foam scale, it can be used for instance to visualize the flow of foam in micromodels with different permeabilities,[22,23] study the hysteretic behavior of foam[24] or the dislocation dynamics in a two-dimensional crystal foam flowing in a tapered channel,[25] control the foamability of surfactants,[16] or investigate the destabilization, propagation, and generation of foam during the movement of crude oil in heterogeneous model porous media.[26] The geometry of the single pore used in our study is similar to that of a planar flow focusing device.[27] Planar flow focusing is a very efficient microfluidic technique used to produce highly monodisperse drops or bubbles.[28−31] It operates on a very basic principle: a 2D coaxial stream made of two immiscible fluids is forced to flow through a small orifice having a rectangular cross-section. Depending on the operating conditions (values of the flow rates or pressure drops used to inject both fluids into the device, surface tension, and viscosity ratio between the two fluids), the flow can destabilize and form periodic trains made up of droplets or bubbles, depending on whether the internal fluid is a liquid or a gas. A considerable amount of work has been devoted over the last two decades to studying the stability of coaxial confined gas (respectively liquid) flows and the dynamics and mechanism of bubble (respectively droplet) formation. Authors have notably theoretically investigated the effect of the channel cross-section (circular[32] or rectangular[33−35]) on the stability of the inner jet.

For rectangular cross-section channels, in the absence of Marangoni effects,[36] the stability of the gas inner thread depends strongly on its degree of geometric confinement. When the width of the jet is greater than the height of the channel, H, the Rayleigh−Plateau instability due to surface tension[37] is suppressed so that the gas flow is absolutely stable and never collapses into bubbles, unlike what happens when its width becomes less than H.[33,34,36] Note that if the gas is replaced by a liquid, the same phenomenon is witnessed.[35] For experiments performed at constant gas pressure, as the width decreases as the liquid flow rate increases, the inner gas jet becomes unstable above a critical value of the flow rate, generating a foam made of monodisperse bubbles. The bubble formation mechanism, for its part, still remains not fully understood as it results from a subtle interplay between inertial and interfacial effects as well as the geometry of the microfluidic device[29,38−42] and requires a complete hydrodynamic description of the pinching process.[43,44] Surprisingly, although the mechanisms of gas jet destabilization leading to bubble formation in planar flow focusing devices are now well documented, no microfluidic study to our knowledge conducted with such devices has yet investigated and rationalized the destabilization of the foam produced when it becomes too dry (i.e., when $f_g \geq f_g^*$), resulting in the formation of a continuous gas flow. Our present work aims to fill this gap and answer the three following questions: (1) What are the physical mechanisms underlying the collapse of foam produced by a flow-focusing device? (2) What are the physical parameters that control the maximum volume fraction of bubbles, f_g^*, that can be observed? (3) For a given geometry of the flow-focusing device, can we predict the value of f_g^*?

2. MATERIALS AND METHODS

2.1. Experimental Setup. We carry out our experiments working with planar microfluidic devices made of poly(dimethylsiloxane) (PDMS) transparent elastomers. These devices are fabricated using standard soft lithography

https://doi.org/10.1021/acsomega.3c09071
ACS Omega 2024, 9, 8320−8332

techniques[19] by using a SmartPrint apparatus (from SmartForce Technologies, France). A mold of PDMS (Sylgard 184 Silicone Elastomer, Dow Corning) is sealed to a glass slab covered with PDMS previously treated using a plasma cleaner to achieve also the hydrophilicity of the channels. As this treatment is not permanent, a new microfluidic device is used for each experiments. The width and height of the channels are, respectively, W_m = 400 μm and H = 76 μm. Bubbles are generated using a flow focusing geometry (FFG),[28] whose characteristics are depicted in the Figure 1 caption. The width of the constriction and its length are given as W_c and L_c, respectively. We investigate the effect of the FFG on the generation of bubbles by working with L_c = 600 μm for three different values of W_c, namely 100, 200, and 250 μm. In such devices, there are three inlet channels: the two outer channels delivers the liquid at a net flow rate $\frac{Q_w}{2}$ each, supplied from a syringe pump Nexus 3000 (Chemyx, USA). Gas (Nitrogen) is injected through the central inlet from a pressurized tank whose pressure P_g is controlled by means of pressure controller OB1 MK3 + (Elvesys, France). The main channel outlet, located at a distance L_m = 2.35 cm downstream the FFG is at atmospheric pressure, P_0. The setup is placed under an inverted microscope DM IL LED (Leica, Germany) with a 5−10× objective, which is connected to a high-speed camera Fastcam Mini AX100 (Photron, Japan). The rate of acquisition is 20000 frames per second, and the field of view is 600 × 1200 μm^2. All our experiments are performed at T = 23 °C. In our experiments, we perform cycling variations of Q_w while maintaining the value of the P_g constant at either 1.3 or 1.4 bar. For each value of Q_w, once a steady state is reached, we record images of the flow in the main channel and in the FFG, and we measure the pressure drop ΔP with 2 pressure sensors MPS1 (from Elvesys, France) over a portion of the main channel of length, L_p = 1.7 cm located downstream the cross-junction, with an measurement error smaller than 1 mbar. We check the reproducibility of our observations and data by performing each experiments thrice. The gas flow rate Q_g is measured with two gas flowmeters El-Flow Select F-111B and F-110C (from Bronkhorst, USA), connected in series in order to cover a sufficient range of measurement. Videos of the flow are analyzed with ImageJ software and a custom-written MATLAB image processing software to determine either the bubble production rate, f_{prod} or the width d_c of the gas stream in the constriction when no bubbles are formed. Since when foam generation occurs, monodisperse bubbles are periodically emitted; their volume Ω is determined from the measured values of Q_g, and f_{prod}, accordingly to the following relationship $\Omega = \frac{Q_g}{f_{prod}}$. For each set ($P_g$, Q_w) of imposed flow variables, the gas volume fraction is determined from the measured value of Q_g according to $f_g = \frac{Q_g}{Q_g + Q_w}$.

2.2. Chemical Systems. Foams are produced in our microfluidic devices by coinjecting nitrogen and a surfactant solution that contains 1 wt % of Tween 20, a nonionic surfactant (Sigma-Aldrich) solubilized in a brine solution (1 g L^{-1} of NaCl). The values of the Newtonian viscosity, η, and the gas/liquid surface tension, γ, which have been determined at T = 23 °C using respectively a low-shear rheometer LS300 (from proRheo, Germany) and a tensiometer TRACKER (from TECLIS, France) based on a pendant drop method, are η_w = 0.95 mPa s and γ_w = 33.6 mN m^{-1}. The nitrogen viscosity is η_g = 0.0177 mPa s at T = 23 °C and atmospheric pressure.

2.3. Numerical Calculations. We numerically solve the Navier−Stokes equation to determine, in both the gas and the liquid, the 3D velocity profile and the corresponding pressure gradient $\left(\frac{dP}{dx}\right)_c$ for a steady-state regime for which an inner gas/liquid coflow stream with width d_c flows in a channel having a constant rectangular cross-section $H \times W_c$ (with $H \leq W_c$), a configuration that corresponds to our experimental device. Calculations are carried out assuming that (i) both fluids are Newtonian, (ii) the flow is incompressible (the Mach number at play for each fluids is very small), (iii) the liquid wets the surfaces of the channels, (iv) no Marangoni effects are present (i.e., there is no gradient of surfactant molecules so that the surface tension is considered constant), and (v) the Reynolds numbers at play are small enough so that the flow is laminar. These approximations have proved well suited to the description of 2D coaxial flows.[35,45]

For each fluid, the mass conservation and the Stokes equation are then written, respectively

$$\text{div}\ \vec{u_i} = 0 \tag{1}$$

and

$$\eta_i \Delta \vec{u_i} = \overrightarrow{\text{grad}} P_i \tag{2}$$

where $\vec{u_i}$, η_i, and P_i stand for the velocity, viscosity, and pressure field within fluid i, respectively. The indexes i = 1 and i = 2 correspond, respectively, to the gas and the liquid phases. As the flow field is unidirectional for both fluids, it can be written as $\vec{u_i} = U_i(x, y, z)\vec{e_x}$, where x is the direction of the flow.

Because of the Young−Laplace equation, the pressure fields in both fluids satisfy the following relationship

$$P_1(x) - P_2(x) = \frac{\gamma}{R(x)} \tag{3}$$

where $R(x)$ is the radius of curvature of the interface. In the steady-state coflow regime, the pressure gradients in both fluids are equal as $R(x)$ is constant along the flow direction, so

$$\frac{\partial P_1}{\partial x} = \frac{\partial P_2}{\partial x} \tag{4}$$

We investigate both 2D-confined and 3D-unconfined situations for which the width of the gas stream, d_c, is larger or smaller than H, respectively. For a 2D-confined situation, the cross-section of the gas stream in the (y, z) plane is modeled in a good approximation by a rectangle of dimensions $H \times (d_c - H)$ bounded with two-half circles of radius $\frac{H}{2}$, as illustrated in Figure 2, so that $R(x) = \frac{H}{2}$. In contrast, for a 3D-unconfined situation, the cross-section of the gas stream is circular with a radius $R = \frac{d_c}{2} \leq \frac{H}{2}$.

The previous set of equations is closed by using (i) a no-slip boundary condition at the wall for each fluids, (ii) the continuity of the velocity at Σ, the gas/fluid interface, and (iii) that of the shear stress, which is written as

$$\eta_1 \frac{\partial U_1}{\partial \vec{n}} = \eta_2 \frac{\partial U_2}{\partial \vec{n}} \tag{5}$$

where $\vec{n}$ is the normal vector to Σ.

https://doi.org/10.1021/acsomega.3c09071
ACS Omega 2024, 9, 8320−8332

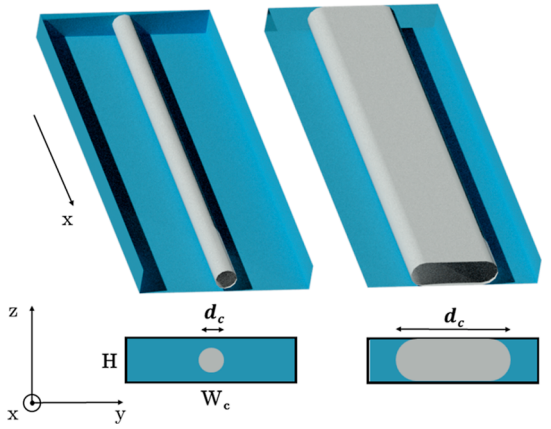

Figure 2. Top: 3D schematic views of the gas jet in the constriction of the FFG corresponding to 3D-unconfined and 2D confined configurations, respectively. Bottom: Schematic sketch of the cross-section of the gas jet in the (y, z) plane. x is the direction of the flow. L_c is the length of this channel portion.

By using the fluid incompressibility condition, it is straightforward to show that the velocity fields in both fluids do not depend on the x variable and that both pressure gradients along the x direction are constant and equal to $\left(\frac{dP}{dx}\right)_c = \frac{\Delta P_c}{L_c}$, where ΔP_c is the pressure drop measured over the length channel portion, L_c. For given set of values $\left(\left(\frac{dP}{dx}\right)_c, d_c\right)$, it is therefore possible to solve the previous set of equations to determine the velocity profiles and hence the flow rates of both fluids, according to

$$Q_i = \iint_{\mathcal{V}_i} U_i(y, z)\mathrm{d}y\mathrm{d}z \tag{6}$$

where $\mathcal{V}_i$ is the domain of fluid i.

Numerical calculations are performed by using a Cartesian regular mesh and a finite volume discretization of the equations.[46] The computation code was developed by T. Colin under Scilab, a free scientific software developed by INRIA, France. A rapid dimension analysis of the problem permits showing that

$$Q_w = \frac{H^4}{\eta_w} G\left(\frac{\eta_g}{\eta_w}, \frac{W_c}{H}, \frac{d_c}{H}\right) \times \left(\frac{dP}{dx}\right)_c \tag{7}$$

and

$$Q_g = \frac{H^4}{\eta_g} K\left(\frac{\eta_g}{\eta_w}, \frac{W_c}{H}, \frac{d_c}{H}\right) \times \left(\frac{dP}{dx}\right)_c \tag{8}$$

where G and K are two functions of dimensionless parameters.

From these two equations, one straightforwardly demonstrates that the dimensionless width of the gas jet $\frac{d_c}{H}$ is a function of the three dimensionless parameters, $q = \frac{Q_g}{Q_w}$, $\eta = \frac{\eta_g}{\eta_w}$, and $A = \frac{W_c}{H}$ and therefore writes

$$\frac{d_c}{H} = F(q, \eta, A) \tag{9}$$

We numerically predict the variation of $\frac{d_c}{H}$ as a function of q for a given channel geometry and for $\eta = 0.0186$ as follows: for a given set $\left(d_c, \left(\frac{dP}{dx}\right)_c\right)$, the corresponding velocity profiles in both fluids are computed, and from these profiles the values of Q_w and Q_g (and hence of q) are determined. By systematically varying d_c and $\left(\frac{dP}{dx}\right)_c$, we can then extract from our computed data set $\frac{d_c}{H}$ as a function of Q_w for different values of Q_g (or vice versa) and therefore as a function of either q or $f_g = \frac{q}{1+q}$, the gas volume fraction. The results are presented in Section 3.3.

3. EXPERIMENTAL RESULTS

3.1. General Observations: Steady States and Bistability. We start by reporting observations made in the constriction of the FFG, for which $W_c = 200$ μm, when for a given value of $P_g = 1.3$ bar, the value of Q_w is continuously increased, starting from a minimum value of $Q_w = 20$ μL/min. Experimentally, we identified two different steady-state regimes. For low values of Q_w, a stable gas/liquid coflowing stream forms in the central part of constriction (regime I). The width of this gas jet, d_c, continuously decreases as Q_w increases until, for a critical flow rate value, $Q_{I\to II}$, the gas jet pinches and breaks into monodisperse bubbles that are periodically emitted at a locus found in the constriction (regime II) (see Figure 3). The value of

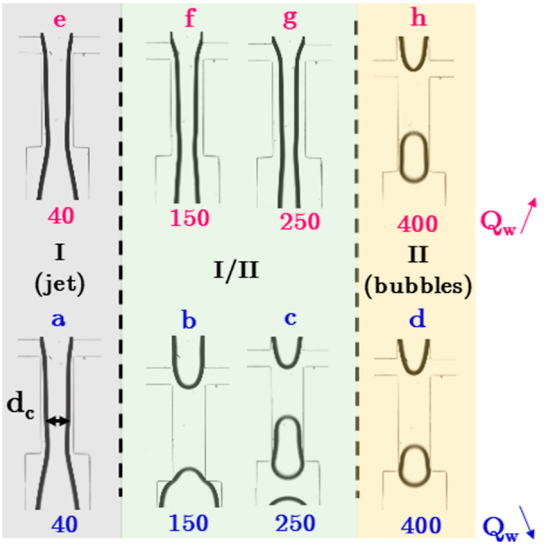

Figure 3. Images of the two-phase flow observed in the main channel downstream the FFG for different values of Q_w (given in μL/min) when continuously increasing (pink, top) or decreasing (blue, bottom) Q_w. The value of P_g is 1.3 bar.

$Q_{I\to II}$ is very reproducible. As shown in Figure 4, in regime I, ΔP linearly increases with Q_w while Q_g linearly decreases. In the bubble region (regime II), the values of ΔP and Q_g remain almost constant. The transition between the gas jet and the bubbles is accompanied by jumps in the measured values of ΔP and Q_g.

In our experiments carried out at a given value of P_g, once the foam has formed (regime II), we then slowly and continuously decrease Q_w, taking care to reach a stable state for each value of Q_w applied, and then measuring the values of ΔP and Q_g, whose variations with Q_w (shown in blue symbols) are plotted in Figure

https://doi.org/10.1021/acsomega.3c09071
ACS Omega 2024, 9, 8320−8332

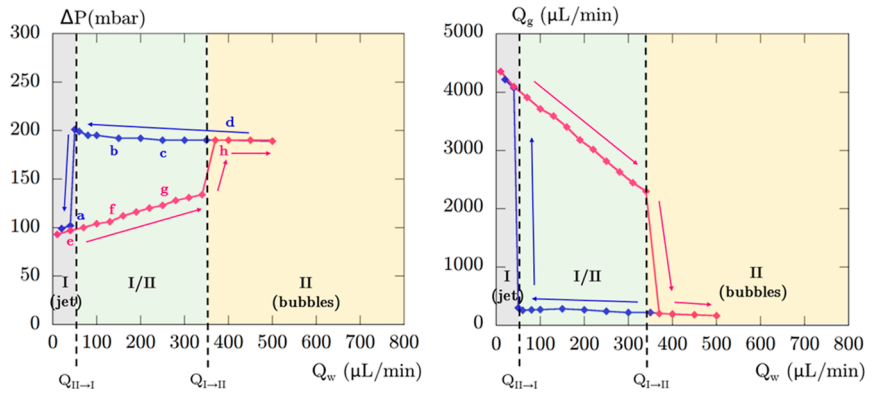

Figure 4. Left: Pressure drop measured as a function of Q_w over a portion length L_p = 1700 μm of the main channel (width W) when increasing (pink) or decreasing (blue) the liquid flow rate for the geometry with W_c = 200 μm and P_g = 1.3 bar. Right: Gas flow rate measured as a function of Q_w when increasing (pink) or decreasing (blue) the liquid flow rate for the same geometry.

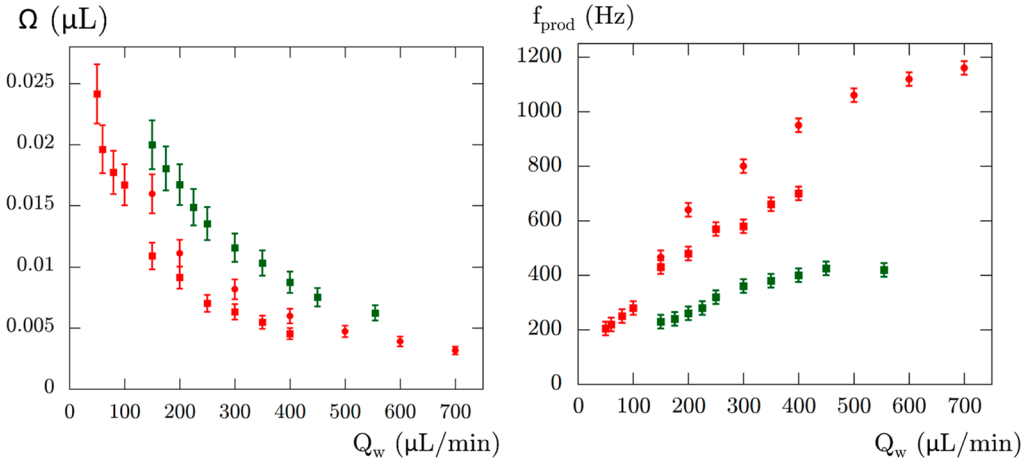

Figure 5. Evolution of the volume of the bubbles (left) and frequency of generation of bubbles (right) with Q_w for the 3 experiments: P_g = 1.3 bar and W_c = 200 μm (red box solid), P_g = 1.3 bar and W_c = 250 μm (green box solid), and P_g = 1.4 bar and W_c = 200 μm (red circle solid).

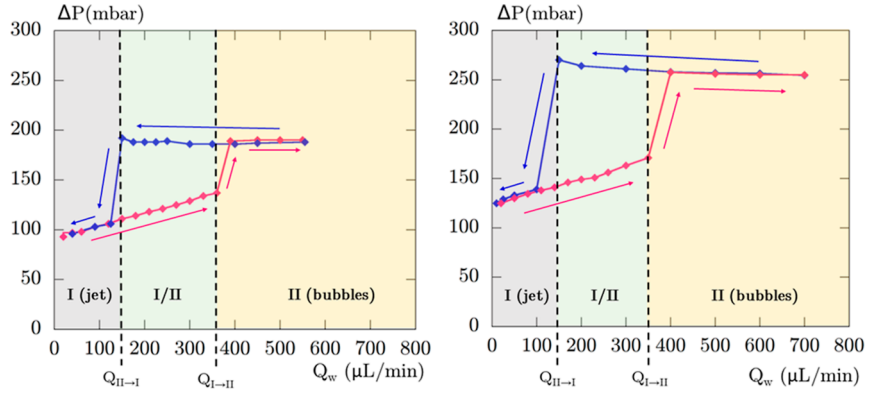

Figure 6. Pressure drop measured as a function of Q_w over a portion length L_p = 1700 μm of the main channel when increasing (pink) or decreasing (blue) the liquid flow rate for the chips with W_c = 250 μm and 1.3 bar (left) and with W_c = 200 μm and P_g = 1.4 bar (right).

4. Surprisingly, we witness the existence of a bistability region, where either a jet or bubbles are observed (Figure 3), depending on how the region is entered. Note that the values of the pressure drops that are measured in this region significantly differ depending on whether a gas jet or bubbles are observed. In regime II, as Q_w decreases, the volume of the bubbles that are produced, Ω, increases in contrast to their production rate, f_{prod} (see Figure 5). Note also that as Q_w decreases, ΔP slightly increases as the produced foam becomes drier (see Figure 4). Below a critical liquid flow rate of $Q_{II\to I} < Q_{I\to II}$, the foam is no longer observed, and instead a gas jet forms (regime II) whose width increases as Q_w decreases. In this region, for a given value of Q_w, the values of ΔP and Q_g, as well as those of d_c, are the same whether the experiments are carried out by increasing or decreasing the liquid flow rate. The existence of these two steady states separated by a region of bistability is a very general and robust phenomenon, as we observe it with different flow

https://doi.org/10.1021/acsomega.3c09071
ACS Omega 2024, 9, 8320−8332

focusing geometries and different values of P_g, as displayed in Figure 6.

3.2. Transition I → II between Gas Stream and Bubbles. To gain a physical understanding of the origin of the transition between the I and II regimes, which occurs when $Q_w = Q_{I\to II}$, we study regime I in more detail by visualizing the flow in the constriction of the FFG, where the gas flow pinches and forms bubbles. As shown in Figure 7, in this regime, the steady state width of the jet d_c decreases as Q_w increases while $d_c > H$. In this configuration, if we neglect the thickness of the lubrication film between the gas and the top and bottom walls of the channel, the cross-section of the gas jet can be well approximated, as depicted in Figure 2, by a rectangle of dimension $H \times (d_c - H)$ bounded by two half-cylinders of radius $H/2$. This is valid because the capillary numbers involved in our experiments are small (typically on the order of 10^{-2}). Recall that the thickness of the lubrication film scales as $HCa^{2/3}$, where $C_a = \frac{\eta_w V}{\gamma}$ is the capillary number at play (in this expression, V represents the mean fluid velocity).[47] For such a 2D-confined configuration, a perturbation of the width of the gas jet, $\delta d_c(x, t)$ along x, the flow direction, leads to a Laplace pressure perturbation term, $\delta P(x, t)$, that, in the absence of Marangoni effects, is always stabilizing as it writes $-\gamma\frac{\partial^2 d_c}{\partial x^2}$ (the radius of curvature of the gas/liquid interface along its normal remains constant as it equals to $H/2$).[33,34,36] For this reason, as previously noted by Dollet et al.,[33] we experimentally witness the formation of bubbles only when d_c becomes equal to H, that is, when the cylindrical jet adopts a circular cross-section, a geometry that is unstable with respect to the surface tension-driven Rayleigh-Plateau instability.[37]

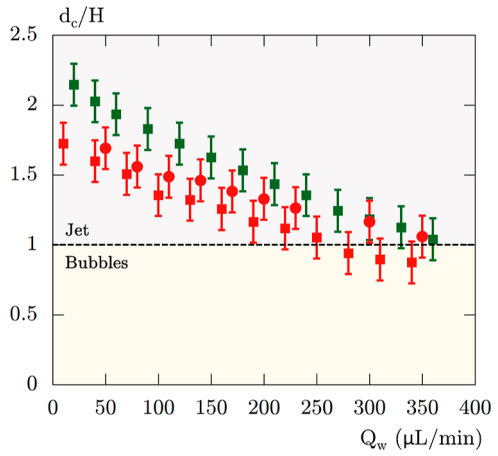

Figure 7. Variation of the ratio width of the jet in the constriction/channel height $\frac{d_c}{H}$ with Q_w during the increasing Q_w variation (pink in Figure 6) for the 3 experiments: $P_g = 1.3$ bar and $W_c = 200\ \mu$m (red box solid), $P_g = 1.3$ bar and $W_c = 250\ \mu$m (green box solid), and $P_g = 1.4$ bar and $W_c = 200\ \mu$m (red circle solid).

3.3. Numerical Simulations: Results and Comparisons with Experimental Findings. We take this analysis a step further by carrying out numerical simulations to now solve numerically the Navier−Stokes equations to determine the 3D velocity profiles and corresponding pressure gradient $\left(\frac{dP}{dx}\right)_c$ for the above steady-state configuration (a central jet in a rectangular channel). These numerical calculations are performed for both 2D-confined and 3D-unconfined situations (although the 3D situation is unstable with respect to the Rayleigh-Plateau instability and therefore cannot be experimentally observed) following the procedure described in detail in Section 2.3. Briefly, the numerical solution of the Navier−Stokes equation requires two input variables, which are d_c and the pressure gradient $\left(\frac{dP}{dx}\right)_c$. In the steady state, this pressure gradient is uniform and identical in the liquid and in the gas. By proceeding in this way, the numerical resolution allows one to first determine the velocity profile in both phases and then the two output variables: Q_w and Q_g. From the obtained data set, it is possible for a given geometry to extract and plot $\frac{d_c}{H}$ as a function of $\left(\frac{dP}{dx}\right)_c$ for different values of Q_w, as shown in Figure 8. Very interestingly, as expected from a dimensional analysis of the problem (see Section 2.3 for a full discussion), we remark that

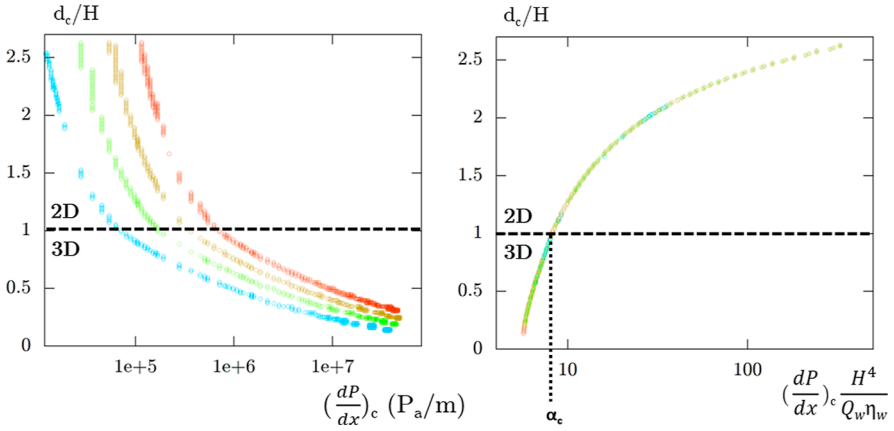

Figure 8. Left: variation of $\frac{d_c}{H}$ with $\left(\frac{dP}{dx}\right)_c$, numerically obtained for the same channel height $H = 76\ \mu$m and channel width $W_c = 200\ \mu$m, but different values of Q_g: 200 (green circle open), 500 (green circle open), 1000 (brown circle open), and 2000 (brown circle open) μL/min. Right: variation of $\frac{d_c}{H}$ with $\left(\frac{dP}{dx}\right)_c \times \frac{H^4}{\eta_w Q_w}$, numerically obtained for the same channel height $H = 76\ \mu$m and channel width $W_c = 200\ \mu$m, and same Q_g as left. Error bars are smaller than the size of the symbols used to represent numerical data.

https://doi.org/10.1021/acsomega.3c09071
ACS Omega 2024, 9, 8320−8332

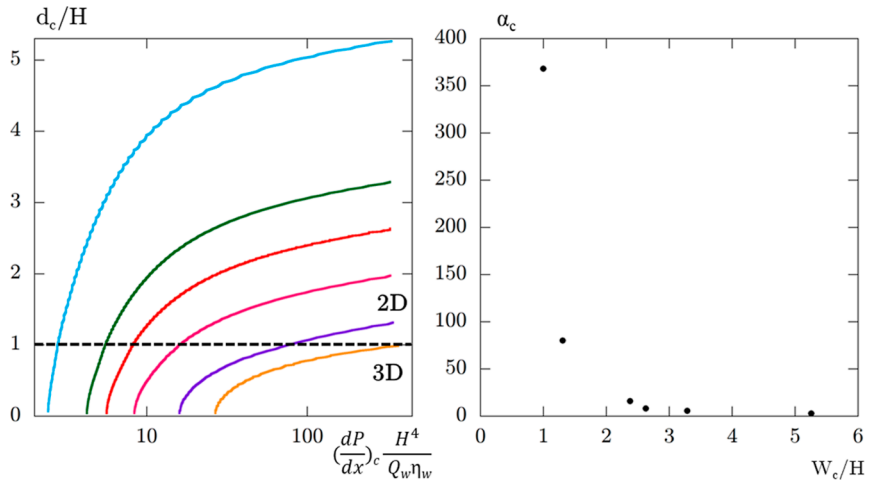

Figure 9. Left: variation of $\frac{d_c}{H}$ with $\left(\frac{dP}{dx}\right)_c \times \frac{H^4}{\eta_w Q_w}$, numerically obtained for the same channel height, H = 76 μm, but different values of the channel width W: 76 (orange), 100 (purple), 150 (pink), 200 (red), 250 (green), and 400 (blue) μm. Right: variation of α_c with W_c/H. Error bars are smaller than the size of the symbols used to represent numerical data.

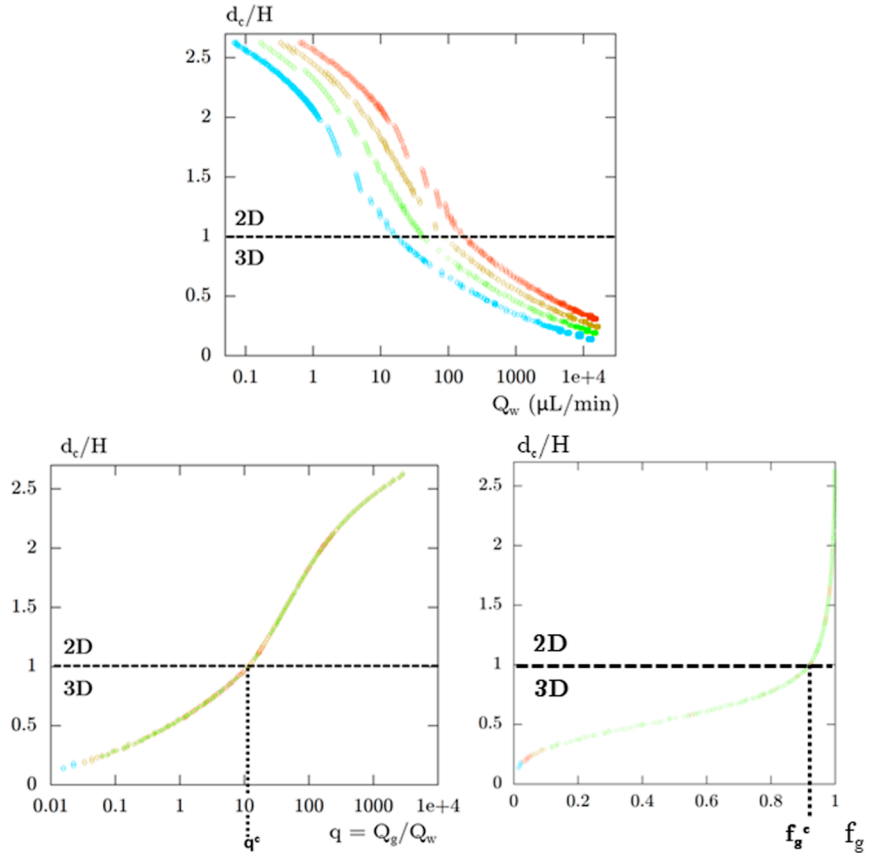

Figure 10. Top: variation of $\frac{d_c}{H}$ with Q_w, numerically obtained for the same channel height H = 76 μm and channel width W_c = 200 μm, but different values of Q_g: 200 (blue circle open), 500 (green circle open), 1000 (yellow circle open), and 2000 (red circle open) μL/min. Bottom left: variation of $\frac{d_c}{H}$ with $q = \frac{Q_g}{Q_w}$, numerically obtained for the same channel height H = 76 μm and channel width W_c = 200 μm represented for the same data in the left graph. q^c is the value of q for which $d_c = H$. Bottom right: variation of $\frac{d_c}{H}$ with f_g numerically obtained for the same channel height H = 76 μm and channel width W_c = 200 μm represented for the same data of the left graph. f_g^c is the value of f_g for which $d_c = H$. Error bars are smaller than the size of the symbols used to represent numerical data.

https://doi.org/10.1021/acsomega.3c09071
ACS Omega 2024, 9, 8320−8332

when we plot $\frac{d_c}{H}$ as a function of $\left(\frac{dP}{dx}\right)_c \times \frac{H^4}{\eta_w Q_w}$, all numerical data collapse on a master curve, as evident in Figure 8. Such a master curve demonstrates that for a given geometry of the channel and a given value of Q_w, there exists a critical pressure gradient, $g_c^c = \alpha_c \frac{\eta_w Q_w}{H^4}$ with α_c being a numerical constant that depends on the asymmetry of the channel, i.e., on the ratio $\frac{W_c}{H}$, for which $\frac{d_c}{H} = 1$, as shown in Figure 9. This value determines the transition between a steady-state 2D-confined gas and an unsteady state that leads to the formation of bubbles. When $\left(\frac{dP}{dx}\right)_c > g_c^c$, the jet which is 2D-confined is stable, whereas when $\left(\frac{dP}{dx}\right)_c \leq g_c^c$, it is 3D-unconfined and therefore breaks into bubbles as a result of the Rayleigh-Plateau instability. As we have no experimental measurements of the pressure gradient in the constriction of our device, where fragmentation of the jet into bubbles occurs, it is not possible to compare our aforementioned numerical predictions above with experimental results. However, as detailed below, we can test the validity of the numerical model by comparing the numerically predicted jet width for different values of Q_w and Q_g with our experimental data.

In fact, following the procedure described in Section 2.3, it is also possible from the previously obtained numerical data to determine $\frac{d_c}{H}$ for various values of Q_g and Q_w (see Figure 10). Note that to compare our numerical results with experimental findings, the values of W_c and H are chosen to match the widths of the constriction and the channel height $H = 76$ μm of our microfluidic devices used to gather the data reported in Figure 7. We start by investigating the case of $W_c = 200$ μm. As theoretically expected (see Section 2.3 for an extended discussion), we observe that all these numerical data collapse on a master curve when one plots $\frac{d_c}{H}$ as a function of $q = \frac{Q_g}{Q_w}$ (see Figure 10). For a given geometry, the bubble/jet transition occurs for a specific value of q (respectively f_g), which, in the following, we name q^c (resp f_g^c). Remarkably, as reported in Figure 11, we note that for the two geometries investigated in our study (namely, $W_c = 200$ and $W_c = 250$ μm), our experimental data relatively well collapse on the numerically predicted master curves (red and green curves), although there is some noticeable discrepancy when the width of the gas stream becomes large. Such a discrepancy is likely due to Marangoni effects and the presence of Bretherton films that we neglect in our approximated model. Nevertheless, despite its simplicity and the crude assumptions made, our basic model seems to offer a relatively good description of our experimental findings for narrow 2D-confined gas jets.

For a given H value and a fixed q value, the smaller the channel width, the smaller the jet width predicted by the model. Consequently, for a planar device made up of serially assembled channels of different widths but the same height, the destabilization of a continuous stationary gas jet should always take place in the narrowest part of the circuit, as observed experimentally. Although this result is well known to experimenters, the model provides numerical proof of it. Finally, our numerical results show that the dimensionless steady-state width of the gas jet depends on the ratio $q = \frac{Q_g}{Q_w}$ and henceforth on the gas volume fraction $f_g = \frac{q}{1+q}$. In the absence of

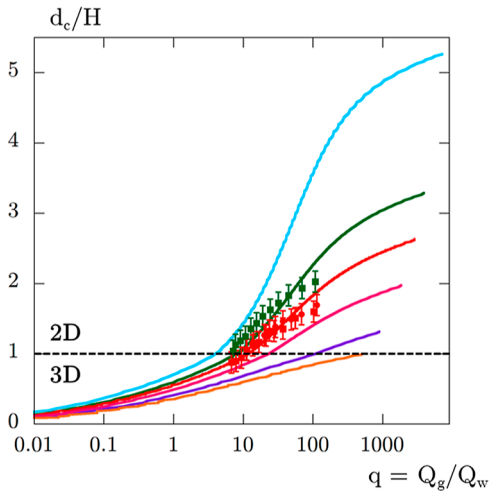

Figure 11. Variation of $\frac{d_c}{H}$ with $q = \frac{Q_g}{Q_w}$, numerically (lines) obtained for the same channel height, $H = 76$ μm, but different values of the channel width W_c: 76 (orange), 100 (purple), 150 (pink), 200 (red), 250 (green), and 400 (blue) μm. Values obtained experimentally for the experiments with $P_g = 1.3$ bar and $W_c = 200$ μm (red box solid), $P_g = 1.3$ bar and $W_c = 250$ μm (green box solid), and $P_g = 1.4$ bar and $W_c = 200$ μm (red circle solid). Lines end at the point corresponding to $d_c = W_c$, as the numerical simulations are possible only until here. Error bars are smaller than the size of the symbols used to represent numerical data.

Marangoni effects, a gas jet is unstable when it becomes 3D-unconfined, that is to say, when $\frac{d_c}{H} = 1$.[33,34,36] Subsequently, for a given FFG, there exists a critical gas volume fraction, $f_g^c = \frac{q^c}{q^c+1}$, below which only a foam can be witnessed. A quick glance at Figure 11 reveals that for a fixed value of H, f_g^c is a decreasing function of W_c whose maximum value, reached for a square cross-section of 0.998, is very close to 1. Experimentally, we remark that the values of $f_g^{I\to II}$ (respectively $q^{I\to II}$) at which the transition I → II occurs correspond to the values f_g^c (respectively q^c), numerically predicted (see Figure 11).

3.4. Transition II → I and Geometric Limitation of the Bubble Volume Fraction. We now take a closer look at the destabilization of the foam (transition II → I). Working with different flow focusing geometries, for a given value of P_g, starting from $Q_w > Q_{I\to II}$, we continuously decrease the value of Q_w while measuring Q_g, and hence, $f_g = \frac{Q_g}{Q_g+Q_w}$, making sure that bubbles are still produced until $Q_w = Q_{II\to I}$ the foam collapses, and a continuous gas stream is witnessed (see Figures 3 and 4). As shown in Figure 12, for all experiments conducted by varying the pore geometry while working with a fixed value of P_g, we observe that as Q_w decreases, the foam becomes drier and drier and the bubbles become coarser and coarser. In Figures 13 and 14, we show as a function of f_g the evolution of the foam texture observed in the main channel corresponding to the data presented in the left and right graphs of Figure 12, respectively. From these data, we determine the maximum bubble volume fraction that can be produced for a foam $f_g^{II\to I}$ with different geometries. As shown on the right of Figure 12, the value of $f_g^{II\to I}$ seems not to depend on P_g. However, it is strongly affected by the geometric parameters of the FFG (Figure 12 left). Note that the determination of $f_g^{II\to I}$ is sensitive to noise because of

https://doi.org/10.1021/acsomega.3c09071
ACS Omega 2024, 9, 8320−8332

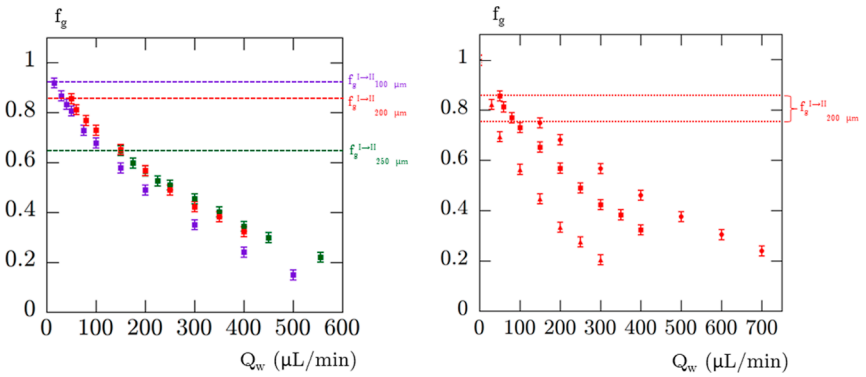

Figure 12. Left: variation of f_g in the decreasing phase (blue in Figure 6), for 3 experiments with the same P_g = 1.3 bar but 3 different W_c: 100 μm (violet box solid), 200 μm (red box solid), and 250 μm (green box solid). Right: variation of f_g in the decreasing phase for 3 experiments with the same W_c = 200 μm but 3 different P_g: 1.2 bar (red triangle up solid), 1.3 bar (red box solid), and 1.4 bar (red circle solid).

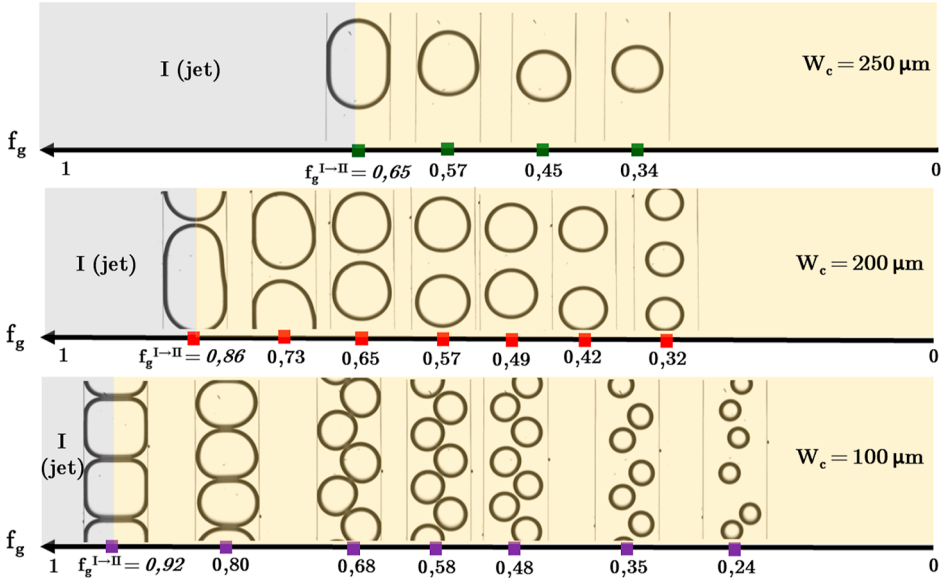

Figure 13. Images of the bubbles at different f_g in the decreasing phase (blue in Figure 6) for 3 experiments with the same P_g = 1.3 bar but 3 different W_c: 100 μm (violet box solid), 200 μm (red box solid), and 250 μm (green box solid). Images stop when regime I (jet) begins. Error bars can be found in Figure 12.

the hysteretic behavior of the system. Finally, as reported in Figure 15, we can see that the $f_g^{II\to I}$ values are relatively close to those of f_g^c, but still lower than them. In Figures 13 and 14, we show as a function of f_g the evolution of the foam texture observed in the main channel corresponding to the data presented in the left and right graphs of Figure 12, respectively. We notice that, in most of the cases, the collapse of the foam occurs even though the bubbles in the main channel are not touching each other and therefore cannot coalesce. This finding, which sharply contrasts with the commonly proposed scenario for the sudden collapse of foams witnessed in real 3D porous media[15] calls for clarification. In the following paragraph, we propose a scenario based on hydrodynamic feedback to explain this phenomenon.

3.5. Discussion About the Bistability Phenomenon and Foam Collapse. As previously explained, the formation of bubbles always occurs in the constriction of our device, which is the narrowest part of the circuit. Numerically, we have shown that at this location, the stability of a steady gas jet is determined by the value of the local pressure gradient and, therefore, by the local pressure drop, ΔP_c. Regime I (stable jet) and regime II (no stable jet = bubbles) are, respectively, observed when $\Delta P_c > g_c^c L_c$ and when $\Delta P_c < g_c^c L_c$, where g_c^c is the value of the critical pressure gradient determined in the constriction. Since our experiments are performed at constant P_g and the constriction and main channel are fluidic elements placed in series, it therefore follows that the value of ΔP_c strongly depends on that of ΔP. Experimentally, we notice that in the bistability region, for a given value of Q_w, ΔP measured in the main channel is significantly larger in the presence of foam in this channel than in the presence of a gas/liquid coflow. The presence of foam in the downstream channel can then considerably reduce the value of the pressure drop across the constriction so that ΔP_c becomes less than $g_c^c L_c$ and no gas jet can form, even though a jet would be stable if the main channel were not filled with bubbles. As Q_w is further decreased, the value of $g_c^c = \alpha \frac{\eta_w Q_w}{H^4}$ decreases. Consequently, at some point, ΔP_c may become equal to $g_c^c L_c$, so that a gas stream may become stable again. Our hydrodynamic model, which predicts the shape and stability of a stationary gas jet as a function of the problem's hydrodynamic and geometric variables, very well describes the I → II transition and shows that the bistability observed in our experiments

https://doi.org/10.1021/acsomega.3c09071
ACS Omega 2024, 9, 8320−8332

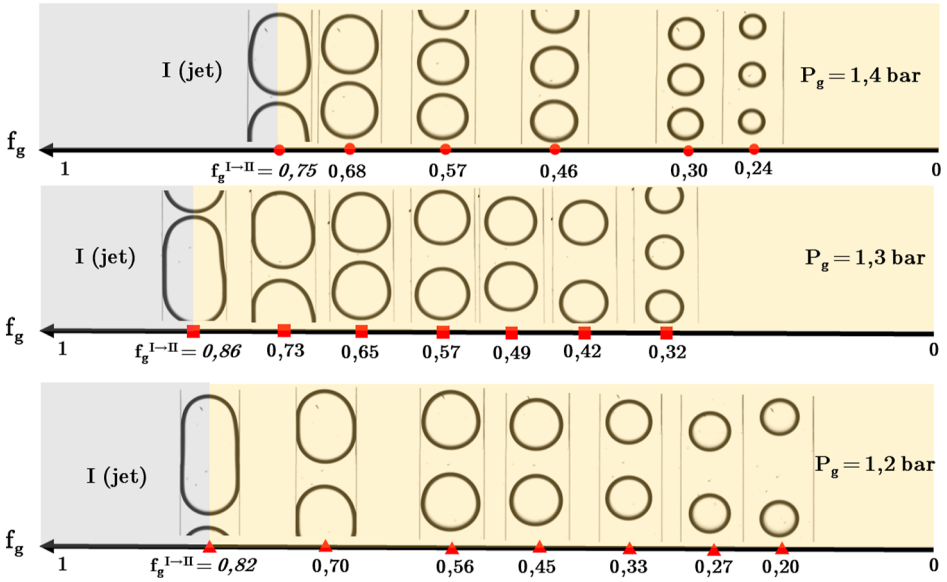

Figure 14. Images of the bubbles at different f_g in the decreasing phase (blue in Figure 6) for 3 experiments with the same $W_c = 200\ \mu m$ but 3 different P_g: 1.2 bar (red triangle up solid), 1.3 bar (red box solid), and 1.4 bar (red circle solid). Error bars can be found in Figure 12.

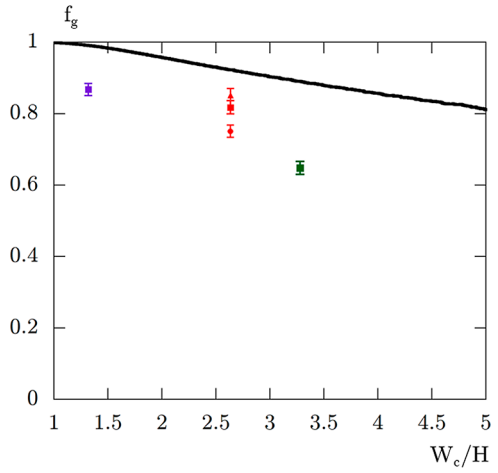

Figure 15. Variation of $f_g^{II\to I}$ measured for our 5 experiments (colors and shapes as in Figure 12) with the ratio $\frac{W_c}{H}$ characterizing the asymmetry of the rectangular section of the FFG used to produce bubbles. We also represent f_g^c (black line) as a function of $\frac{W_c}{H}$. The maximum value of f_g^c reached for $W_c = H$ is 0.998, a value very close to 1.

results from a hydrodynamic feedback mechanism. Unfortunately, it does not allow us to rationalize the transition II → I (i.e., the collapse of the foam) and hence to predict the value of $f_g^{II\to I}$ as bubble formation is a complex dynamic process,[33,48] whose theoretical description is a very difficult task. Nevertheless, our experimental findings clearly indicate that the collapse of the foam in our microfluidic experiments results from a hydrodynamic feedback mechanism and not from coalescence events between bubbles, as usually inferred in the literature.[15] We believe that a similar scenario leads to the hysteretic transition between parallel and Taylor flow recently observed by Chang et al.[49] when using a T-junction to produce foam. Illustrating examples of hydrodynamic feedback processes in microfluidic devices are indeed numerous. For instance, they include traffic of bubbles or drops at a T-junction,[50,51] bistability[52] or multistability phenomena[53] observed in droplet microflows, as well as fragmentation of drops/bubbles past obstacles.[54] Such feedback is also observed with foams produced using microfluidic flow-focusing devices. They lead, for example, to the generation of unstable bubbles[55] or to hysteretic topological transitions between various crystalline foam texture patterns that appear when adjusting gas pressure to a constant liquid flow rate[56] or to a constant fluid pressure.[24] The study of such hydrodynamic feedback is a topical subject that requires systematic studies to understand. Along this line, Labarre and Vigolo[24] have recently studied the influence of various physicochemical parameters (such as liquid viscosity, surface tension, or surface elasticity) on the hysteretic transition observed between bamboo and two-row foams. Our present work falls within this framework.

3.6. Relevance for Foam Flow in Porous Media. In order to put our experimental results into context with those obtained by the industrial community when injecting foam was injected into real porous media, we plotted the effective viscosity η_{eff} that we measured in the main channel as a function of f_g. The value of η_{eff} is determined experimentally from the measured values of the total flow rate $Q_{tot} = Q_g + Q_w$ and ΔP and from the formula giving the expression of the hydrodynamic resistance for a Newtonian fluid in a rectangular cross-section channel according to[57]

$$\eta_{eff} = \frac{\Delta P}{Q_g + Q_w}\frac{H^3 W_m}{12 L_p}\left(1 - 0.63\frac{H}{W_m}\right) \quad (10)$$

As shown in Figure 16, the effective viscosity of the two-phase flow is a single-value function of f_g, exhibiting a maximum of η_{eff}^{max}. For our experiments conducted by decreasing Q_w, we observe that the foam becomes drier (i.e., f_g increases) and that its effective viscosity, η_{eff}, increases up to a point ($f_g = f_g^{II\to I}$), where the foam transforms into a gas continuous stream and the value of η_{eff} sharply drops. This transition is somewhat similar to that reported in porous media between low- and high-quality foams when $f_g = f_g^*$. It is interesting to note that the maximum value of η_{eff} is reached for a value of f_g slightly smaller than $f_g^{II\to I}$.

https://doi.org/10.1021/acsomega.3c09071
ACS Omega 2024, 9, 8320−8332

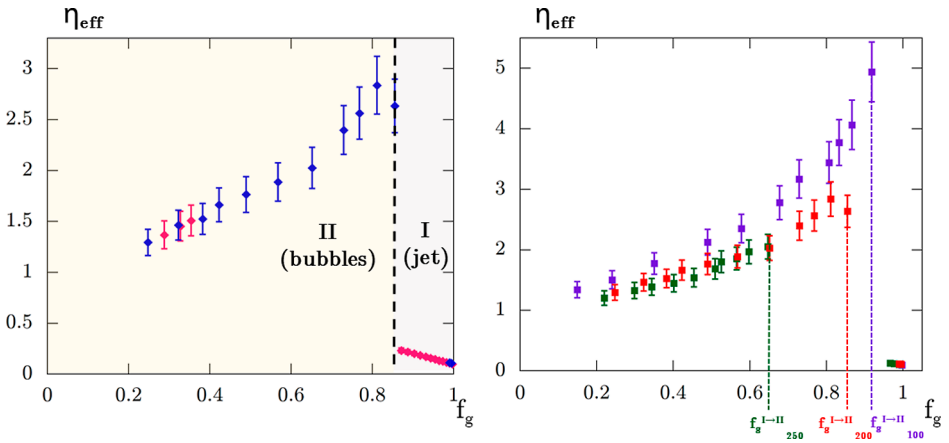

Figure 16. Left: evolution of the effective viscosity of the coflow at different f_g in the decreasing phase (blue) and increasing phase (pink) for the experiment with P_g = 1.3 bar and W_c = 200 μm. Right: evolution of the ratio between the effective viscosity of the coflow and the viscosity of pure water at different f_g in the decreasing phase for 3 experiments with the same P_g = 1.3 bar but 3 different W_c: 100 μm (violet box solid), 200 μm (red box solid), and 250 μm (green box solid).

This feature as well as the variation of η_{eff} with f_g are similar to foam data collected in real porous media (see for instance[10]). Furthermore, in our microfluidic device, as in porous media, the foam bubbles become coarser and coarser as f_g increases.[58] Interestingly, we notice that the values of η_{eff}^{max} increase as the width of the rectangular section pore, W_c, becomes smaller. Such a result finds its explanation in the foam texture that is produced. As shown in Figure 13, close to f_g^*, the size of the bubbles gets smaller as W_c decreases, whereas the foam gets drier. Despite its simplicity, a single flow-focusing device appears to capture relatively well figures of foam flows in porous media and emphasizes the importance of the latter.

4. CONCLUSIONS

In conclusion, we have studied the formation of a foam through FFG (a single-pore microfluidic device) by coinjecting the gas and liquid phases at constant pressure, P_g, and flow rate, Q_w. We have identified the existence of two steady-state regimes: a monodisperse bubble regime and another one in which a stable gas jet flows. As theoretically expected,[33,34,36] we observe that the formation of bubbles always occurs at the pore neck (constriction of the FFG) when the width of the gas jet becomes comparable to the channel height. By performing systematic experiments, tuning the value of Q_w while maintaining the P_g constant has shown that the transition between these two regimes exhibits a bistability region. Using a very simple hydrodynamic model to describe the gas jet flow, we have identified the dimensionless physical parameters of the problem that control the stability of the gas stream and hence the formation of bubbles. By numerically solving this model, we have shown the existence of a critical value of the local pressure drop at the constriction, which determines whether the gas jet is 2D-confined and therefore stable or not. Our experimental findings and numerical simulations demonstrate that the existence of the bistability region results from hydrodynamic feedback due to the presence of downstream bubbles that lower this local pressure drop.

We believe that our results may be important for industrial applications requiring foam injection into soils. It is usually acknowledged that the formation of a continuous gas stream in porous media occurring for high values of gas fractional flows results from the existence of a limiting capillary pressure beyond which the foam coarsens through coalescence events. By studying the mechanism of foam formation through a single pore, we have herein demonstrated that there exists a critical value of the gas fractional flow, $f_g^{II\to I}$, above which the formation of bubbles (and hence of strong foams) is inhibited. The value of $f_g^{II\to I}$ depends only on the geometry of the pore neck. This finding suggests that the value of f_g^* in porous media for which the transition between a strong and a weak foam occurs might not be entirely triggered by a limiting capillary pressure as inferred in the literature[15] but maybe also by a critical gas fraction flow determined by the geometry of the pore necks, $f_g^{II\to I}$. Our results are also of interest to the microfluidic community, as they show that (i) the driest foams produced with a flow-focusing microfluidic device are obtained with a square cross-section of the constriction, and (ii) in a serial assembly of channels having the same height, the destabilization of a gas jet (and therefore the formation of bubbles) always occurs in the narrowest channel. Although this last result is well-known to experimenters, the simplified hydrodynamic model presented herein provides numerical proof of it.

AUTHOR INFORMATION

Corresponding Author

Mattéo Clerget − *TotalEnergies S.E., Pôle d'Etude et de Recherches de Lacq, Lacq 64170, France; Laboratoire Physico-Chimie des Interfaces Complexes, Bâtiment CHEMSTARTUP, Lacq 64170, France;* orcid.org/0000-0003-0712-0008; Email: matteo.clerget@outlook.com

Authors

Alexandra Klimenko − *TotalEnergies S.E., Pôle d'Etude et de Recherches de Lacq, Lacq 64170, France; Laboratoire Physico-Chimie des Interfaces Complexes, Bâtiment CHEMSTARTUP, Lacq 64170, France;* orcid.org/0000-0003-3810-385X

Maurice Bourrel − *Laboratoire Physico-Chimie des Interfaces Complexes, Bâtiment CHEMSTARTUP, Lacq 64170, France*

François Lequeux − *Laboratoire Sciences et Ingénierie de la Matière Molle, ESPCI Paris, Université PSL, Sorbonne Université, Paris 75005, France; Laboratoire Physico-Chimie*

https://doi.org/10.1021/acsomega.3c09071
ACS Omega 2024, 9, 8320−8332

des Interfaces Complexes, Bâtiment CHEMSTARTUP, Lacq 64170, France; orcid.org/0000-0003-4076-3988

Pascal Panizza − *IPR, UMR CNRS 6251, Campus Beaulieu, Université Rennes 1, Rennes 35042, France; Laboratoire Physico-Chimie des Interfaces Complexes, Bâtiment CHEMSTARTUP, Lacq 64170, France;* orcid.org/0000-0003-4738-733X

Complete contact information is available at: https://pubs.acs.org/10.1021/acsomega.3c09071

Notes

The authors declare no competing financial interest.

■ ACKNOWLEDGMENTS

This work was funded by a French CIFRE fellowship (contract number 2020-1424) financed by TotalEnergies S.E. We acknowledge TotalEnergies S.E. management for permission to publish this work. We thank C. Blondeau and N. Passade-Boupat for fruitful discussions. We very warmly acknowledge T. Colin for providing us with the code of the numerical software he developed under Scilab to obtain the 3D velocity profiles of two fluid coflows in a rectangular cross-section channel.

■ REFERENCES

(1) Lake, L. W. *Enhanced Oil Recovery*; Prentice Hall: Englewood Cliffs, 1989.

(2) Mulligan, C. N.; Yong, R. N.; Gibbs, B. F. Remediation technologies for metal-contaminated soils and groundwater:An evaluation. *Eng. Geol.* **2001**, *60* (1−4), 193−207.

(3) Schramm, L. L. Foams:Fundamentals and Applications in the Petroleum Industry. *ACS Advances in Chemistry Series No. 242*; American Chemical Society: Washington DC, 1994.

(4) Andrianov, A.; Farajzadeh, R.; Mahmoodi Nick, M.; Talanana, M.; Zitha, P. L. J. Immiscible Foam for Enhancing Oil Recovery: Bulk and Porous Media Experiments. *Ind. Eng. Chem. Res.* **2012**, *51*, 2214−2226.

(5) Kovscek, A. R.; J.Radke, C. Fundamentals of Foam Transport in Porous Media. *Foams:Fundamentals and Applications in the Petroleum Industry*; Schramm, L. L., Ed.; American Chemical Society: Washington DC, 1993.

(6) Rossen, W. A critical review of Roof snap-off as a mechanism of steady-state foam generation in homogeneous porous media. *Colloids Surf., A* **2003**, *225* (1−3), 1−24.

(7) Hourtane, V.; Bodiguel, H.; Colin, A. Dense bubble traffic in microfluidic loops: Selection rules and clogging. *Phys. Rev. E* **2016**, *93*, 032607.

(8) Cottin, C.; Bodiguel, H.; Colin, A. Drainage in two dimensional porous media: From capillary fingering to viscous flow. *Phys. Rev. E* **2010**, *82* (4), 046315.

(9) Langevin, D. Recent Advances on Emulsion and Foam Stability. *Langmuir* **2023**, *39* (11), 3821−3828.

(10) Jones, S. A.; van der Bent, V.; Farajzadeh, R.; Rossen, W. R.; Vincent-Bonnieu, S. Surfactant screening for foam EOR: Correlation between bulk and core-flood experiments. *Colloids Surf. A Physicochem. Eng. Asp.* **2016**, *500*, 166−176.

(11) Kovscek, A. R.; Radke, C. J. Gas bubble snap-off under pressure-driven flow in constricted noncircular capillaries. *Colloids Surf., A* **1996**, *117* (1−2), 55−76.

(12) Hirasaki, G. J.; Lawson, J. B. Mechanisms of foam flow in porous media: apparent viscosity in smooth capillaries. *SPE J.* **1985**, *25* (02), 176−190.

(13) Gassara, O.; Douarche, F.; Braconnier, B.; Bourbiaux, B. Calibrating and interpreting implicit-texture models of foam flow through porous media of different permeabilities. *J. Pet. Sci. Eng.* **2017**, *159*, 588−602.

(14) Mauray, A.; Chabert, M.; Bodiguel, H. Yield stress fluid behavior of foam in porous media. *Phys. Rev. Fluids* **2020**, *5*, 094004.

(15) Khatib, Z. I.; Hirasaki, G. J.; Falls, A. H. Effects of capillary pressure on coalescence and phase mobilities in foams flowing through porous media. *SPE Reservoir Eng.* **1988**, *3* (03), 919−926.

(16) Micheau, C.; Rosenberg, E.; Barré, L.; Pannacci, N. Microfluidic comparative study of foam flow between a classical and a pH sensitive surfactant. *Colloids Surf., A* **2016**, *501*, 122−131.

(17) Elhag, A. S.; Da, C.; Chen, Y.; Mukherjee, N.; Noguera, J. A.; Alzobaidi, S.; Reddy, P. P.; AlSumaiti, A. M.; Hirasaki, G. J.; Biswal, S. L.; Nguyen, Q. P.; Johnston, K. P. Viscoelastic diamine surfactant for stable carbon dioxide/water foams over a wide range in salinity and temperature. *J. Colloid Interface Sci.* **2018**, *522*, 151−162.

(18) Hatchell, D.; Chen, X.; Daigle, H.; Hartmann, M.; Ordonez-Varela, J.; Blondeau, C.; Johnston, K. Stable CO_2/water foam stabilized by dilute surface-modified nanoparticles and cationic surfactant at high temperature and salinity. *J. Surfactants Deterg.* **2023**, *26*, 421−435.

(19) Duffy, D. C.; McDonald, J. C.; Schueller, O. J. A.; Whitesides, G. M. Rapid Prototyping of Microfluidic Systems in Poly-(dimethylsiloxane). *Phys. Rev. Lett.* **1998**, *70* (23), 4974−4984.

(20) Tian, J.; Kang, Y.; Xi, Z.; Jia, N.; You, L.; Luo, P. Real-time visualization and investigation of dynamic gas snap-off mechanisms in 2-D micro channels. *Fuel* **2020**, *279*, 118232.

(21) Vecchiolla, D.; Giri, V.; Biswal, S. L. Bubble−bubble pinch-off in symmetric and asymmetric microfluidic expansion channels for ordered foam generation. *Soft Matter* **2018**, *14* (46), 9312−9325.

(22) Ma, K.; Liontas, R.; Conn, C. A.; Hirasaki, G. J.; Biswal, S. L. Visualization of improved sweep with foam in heterogeneous porous media using microfluidics. *Soft Matter* **2012**, *8*, 10669−10675.

(23) Lv, M.; Liu, Z.; Jia, L.; Ji, C. Visualizing pore-scale foam flow in micromodels with different permeabilities. *Colloids Surf., A* **2020**, *600*, 124923.

(24) Labarre, L.; Vigolo, D. Microfluidics approach to investigate foam hysteretic behaviour. *Microfluid. Nanofluidics* **2019**, *23*, 129.

(25) Gai, Y.; Leong, C. M.; Cai, W.; Tang, S. K. Spatiotemporal periodicity of dislocation dynamics in a two-dimensional microfluidic crystal flowing in a tapered channel. *Proc. Natl. Acad. Sci. U.S.A.* **2016**, *113* (43), 12082−12087.

(26) Xiao, S.; Zeng, Y.; Vavra, E. D.; He, P.; Puerto, M.; Hirasaki, G. J.; Biswal, S. L. Destabilization, Propagation, and Generation of Surfactant-Stabilized Foam during Crude Oil Displacement in Heterogeneous Model Porous Media. *Langmuir* **2018**, *34*, 739−749.

(27) Anna, S.; Bontoux, N.; Stone, H. A. Formation of dispersions using flow-focusing in microchannels. *Appl. Phys. Lett.* **2003**, *82*, 364−366.

(28) Garstecki, P.; Gitlin, I.; DiLuzio, W.; Whitesides, G. M.; Kumacheva, E.; Stone, H. A. Formation of monodisperse bubbles in a microfluidic flow-focusing device. *Appl. Phys. Lett.* **2004**, *85*, 2649−2651.

(29) Cubaud, T.; Tatineni, M.; Zhong, X.; Ho, C.-M. Bubble dispenser in microfluidic devices. *Phys. Rev.E* **2005**, *72*, 037302.

(30) Engl, W.; Backov, R.; Panizza, P. Controlled production of emulsions and particles by milli and microfluidic techniques. *Curr. Opin. Colloid Interface Sci.* **2008**, *13*, 206−216.

(31) Anna, S. Droplets and bubbles in microfluidic devices. *Annu. Rev. Fluid. Mech.* **2016**, *48*, 285−309.

(32) Guillot, P.; Colin, A.; Utada, A. S.; Ajdari, A. Stability of a Jet in Confined Pressure-Driven Biphasic Flows at Low Reynolds Numbers. *Phys. Rev. Lett.* **2007**, *99*, 104502.

(33) Dollet, B.; van Hoeve, W.; Raven, J.-P.; Marmottant, P.; Versluis, M. Role of the Channel Geometry on the Bubble Pinch-off in Flow-Focusing Devices. *Phys. Rev. Lett.* **2008**, *100*, 034504.

(34) Cabezas, M. G.; Herrada, M. A.; Montanero, J. M. Stability of a jet moving in a rectangular microchannel. *Phys. Rev. E* **2019**, *100*, 053104.

(35) Guillot, P.; Colin, A.; Ajdari, A. Stability of a jet in confined pressure driven biphasic flows at low Reynolds number in various geometries. *Phys. Rev. E* **2008**, *78*, 016307.

(36) Clerget, M.; Klimenko, A.; Bourrel, M.; Lequeux, F.; Panizza, P. Marangoni destabilization of bidimensional-confined gas-liquid co-

flowing streams in rectangular microfluidic channels. *Phys. Fluids* **2023**, *35*, 042111.
(37) Rayleigh, L. On the capillary phenomena of jets. *Proc. R. Soc. London* **1879**, *29*, 71−97.
(38) Fu, T.; Ma, Y.; Funfschilling, D.; Li, H. Z. Bubble formation and breakup mechanism in a microfluidic flow focusing device. *Chem. Eng. Sci.* **2009**, *64*, 2392−2400.
(39) van Hoeve, W.; Dollet, B.; Gordillo, J. M.; Versluis, M.; vanWijngaarden, L.; Lohse, D. Bubble size prediction in coflowing streams. *Europhys. Lett.* **2011**, *94*, 64001.
(40) Lin, X.; Bao, F.; Tu, C.; Yin, Z.; Gao, X.; Lin, J. Dynamics of bubble formation in highly viscous liquid in co-flowing microfluidic device. *Microfluid. Nanofluidics* **2019**, *23*, 74.
(41) Zhang, C.; Weldetsadik, N. T.; Hayat, Z.; Fu, T.; Zhu, C.; Jiang, S.; Ma, Y. The effect of liquid viscosity on bubble formation dynamics in a flow-focusing device. *Int. J. Multiphase Flow* **2019**, *117*, 206−211.
(42) Huang, J.; Yao, Z. Influencing factors and size prediction of bubbles formed by flow focusing in a cross-channel. *Chem. Eng. Sci.* **2022**, *248*, 117228.
(43) van Hoeve, W.; Dollet, B.; Versluis, M.; Lohse, D. Microbubble formation and pinch-off scaling exponent in flow focusing devices. *Phys. Fluids* **2011**, *23*, 092001.
(44) Lu, Y.; Fu, T.; Zhu, C.; Ma, Y.; Li, H. Pinch-off mechanism for Taylor bubble formation in a microfluidic flow-focusing device. *Microfluid. Nanofluidics* **2014**, *16*, 1047−1055.
(45) Guillot, P.; Panizza, P.; Salmon, J.-B.; Joanicot, M.; Colin, A.; Bruneau, C. H.; Colin, T. Viscosimeter on a Microfluidic Chip. *Langmuir* **2006**, *22* (14), 6438−6445.
(46) Eymard, R.; Gallouet, T.; Herbin, R. *Finite Vol. Methods Handbook of Numerical Analysis*; Ciarlet, P. G., Lions, J. L., Eds.; Elsevier, 2000.
(47) Bretherton, F. The motion of long bubbles in tubes. *J. Fluid Mech.* **1961**, *10*, 166−188.
(48) van Hoeve, W.; Dollet, B.; Versluis, M.; Lohse, D. Microbubble formation and pinch-off scaling exponent in flow-focusing devices. *Phys. Fluids* **2011**, *23*, 092001.
(49) Sheng, L.; Li, S.; Wang, K.; Chang, Y.; Deng, J.; Luo, G. Gas-Liquid Microfluidics:Transition Hysteresis Behavior between Parallel Flow and Taylor Flow. *Ind. Eng. Chem. Res.* **2022**, *61*, 18567−18573.
(50) Belloul, M.; Engl, W.; Colin, A.; Panizza, P.; Ajdari, A. Competition between Local Collisions and Collective Hydrodynamic Feedback Controls Traffic Flows in Microfluidic Networks. *Phys. Rev. Lett.* **2009**, *102* (19), 194502.
(51) Belloul, M.; Courbin, L.; Panizza, P. Droplet traffic regulated by collisions in microfluidic networks. *Soft Matter* **2011**, *7*, 9453−9458.
(52) Parthiban, P.; Khan, S. A. Bistability in droplet traffic at asymmetric microfluidic junctions. *Biomicrofluidics* **2013**, *7*, 044123.
(53) Sessoms, D. A.; Amon, A.; Courbin, L.; Panizza, P.; Panizza, P. Complex Dynamics of Droplet Traffic in a Bifurcating Microfluidic Channel: Periodicity, Multistability, and Selection Rules. *Phys. Rev. Lett.* **2010**, *105*, 154501.
(54) Schmit, A.; Salkin, L.; Courbin, L.; Panizza, P. Cooperative breakups induced by drop-to-drop interactions in one-dimensional flows of drops against micro-obstacles. *Soft Matter* **2015**, *11*, 2454−2460.
(55) Sullivan, M.; Stone, H. A. The role of feedback in microfluidic flow-focusing devices. *Philos. Trans. R. Soc., A* **2008**, *366*, 2131−2143.
(56) Raven, J.-P.; Marmottant, P. Periodic microfluidic bubbling oscillator: Insight into the stability of two-phase microflows. *Phys. Rev. Lett.* **2006**, *97*, 154501.
(57) Bruus, H. *Theoretical Microfluidics*; Oxford University Press: New-York, 2008.
(58) Vavra, E.; Puerto, M.; Bai, C.; Ma, K.; Mateen, K.; Biswal, L.; Hirasaki, G. Measuring in-situ capillary pressure of a flowing foam system in porous media. *J. Colloid Interface Sci.* **2022**, *621*, 321−330.

https://doi.org/10.1021/acsomega.3c09071
ACS Omega 2024, 9, 8320−8332